Input timing for spatial processing is precisely tuned via constant synaptic delays and myelination patterns in the auditory brainstem

Annette Stange-Marten[a,1], Alisha L. Nabel[a,b,1], James L. Sinclair[a], Matthew Fischl[a], Olga Alexandrova[a], Hilde Wohlfrom[a], Conny Kopp-Scheinpflug[a], Michael Pecka[a,2], and Benedikt Grothe[a,2]

[a]Division of Neurobiology, Department Biology II, Ludwig-Maximilians-Universitaet Munich, 82152 Planegg-Martinsried, Germany; and [b]Graduate School of Systemic Neurosciences, Ludwig-Maximilians-Universitaet Munich, 82152 Planegg-Martinsried, Germany

Edited by Eric I. Knudsen, Stanford University School of Medicine, Stanford, CA, and approved May 8, 2017 (received for review February 10, 2017)

Precise timing of synaptic inputs is a fundamental principle of neural circuit processing. The temporal precision of postsynaptic input integration is known to vary with the computational requirements of a circuit, yet how the timing of action potentials is tuned presynaptically to match these processing demands is not well understood. In particular, action potential timing is shaped by the axonal conduction velocity and the duration of synaptic transmission delays within a pathway. However, it is not known to what extent these factors are adapted to the functional constraints of the respective circuit. Here, we report the finding of activity-invariant synaptic transmission delays as a functional adaptation for input timing adjustment in a brainstem sound localization circuit. We compared axonal and synaptic properties of the same pathway between two species with dissimilar timing requirements (gerbil and mouse): In gerbils (like humans), neuronal processing of sound source location requires exceptionally high input precision in the range of microseconds, but not in mice. Activity-invariant synaptic transmission and conduction delays were present exclusively in fast conducting axons of gerbils that also exhibited unusual structural adaptations in axon myelination for increased conduction velocity. In contrast, synaptic transmission delays in mice varied depending on activity levels, and axonal myelination and conduction velocity exhibited no adaptations. Thus, the specializations in gerbils and their absence in mice suggest an optimization of axonal and synaptic properties to the specific demands of sound localization. These findings significantly advance our understanding of structural and functional adaptations for circuit processing.

myelination | synaptic transmission delay | sound localization | circuit processing | input timing

Temporal integration of bioelectrical signals via chemical synapses is fundamental to neuronal computations. During circuit processing, neuronal information transfer via action potentials is controlled by exact differences in the occurrence between excitatory and inhibitory inputs (1–5). The arrival time of inputs within circuits in turn is largely shaped by the conduction delay of action potentials along the axons and during synaptic transmission. During ongoing activity, the transmission delays of chemical synapses generally increase in the range of hundreds of microseconds due to short-term adaptations (6–9). However, because temporal integration on postsynaptic neurons usually operates on time scales in the range of milliseconds or even longer (10, 11), sluggishness arising from synaptic mechanisms and axonal conductance is negligible for most of these computations. There are, however, some essential neuronal processing tasks that challenge the temporal precision of our nervous system. For instance, weakly electric fish detect miniature changes in the frequency of a constant electrical field. The neuronal circuits in these animals use electrical instead of chemical synapses in the periphery as a rather unique solution to speed up signal propagation along the first synaptic stages and to allow for stable (i.e., activity invariant) synaptic delays (SDs) (12).

The temporally most precise neuronal computations known in mammals (including humans) occur in the auditory system in circuits processing sound location information (13, 14). Here, individual neurons in the lateral and the medial superior olive (LSO and MSO, respectively) detect coincidences between inputs from the two ears. In both nuclei, this computation is based on precise interactions of glutamatergic excitation and glycinergic inhibition (15, 16), and indeed a subset of the respective inputs is shared between the two circuits (17). One striking shared structural feature is the contralateral inhibitory pathway that is specialized for speed and reliability (Fig. 1*A*). Globular bushy cells (GBCs) in the cochlear nucleus excite glycinergic cells of the medial nucleus of the trapezoid body (MNTB) via highly myelinated and rapidly conducting axons and the giant calyx of Held synapse (18, 19). However, the functional requirements for precise timing of this inhibitory pathway are different for the LSO and MSO circuit: the LSO predominantly computes differences in the relative level of high-frequency sounds between the ears [interaural level difference (ILD)] and shows temporal input precision in the millisecond range for faithful level measurement (13, 20) (see also *Discussion*). In the MSO, on the other hand, microsecond differences in the time of arrival of low-frequency sounds at the two ears [interaural time difference (ITD)] are processed and consequently the requirements for input timing are exceptionally higher (5, 21). Importantly, because the inhibitory pathways involve an additional

Significance

Neural computation depends on precisely timed synaptic inputs, but the way that the timing of inputs is tuned to match postsynaptic processing requirements is not well understood. Here, we studied the same brainstem sound localization pathway in two species with dissimilar temporal processing requirements. Two factors that limit precise timing are synaptic delay and axonal conduction time. In gerbils, which depend on precise timing for sound localization, synaptic delays in fast conducting axons are stable across activity level, and axon myelination is adapted to minimize conduction delays. In mice, which do not depend on precise timing, these specializations are absent. Our results suggest that both axonal and synaptic properties are optimized to the specific functional requirements of neural computation, advancing our understanding of the mechanisms that optimize neural circuits.

Author contributions: M.P. and B.G. designed research; A.S.-M., A.L.N., J.L.S., M.F., O.A., and H.W. performed research; A.S.-M., O.A., C.K.-S., and M.P. analyzed data; M.P. and B.G. jointly supervised this work; and M.P. and B.G. wrote the paper.

The authors declare no conflict of interest.

This article is a PNAS Direct Submission.

Freely available online through the PNAS open access option.

[1]A.S.-M. and A.L.N. contributed equally to this work.

[2]To whom correspondence may be addressed. Email: grothe@lmu.de or pecka@bio.lmu.de.

This article contains supporting information online at www.pnas.org/lookup/suppl/doi:10.1073/pnas.1702290114/-/DCSupplemental.

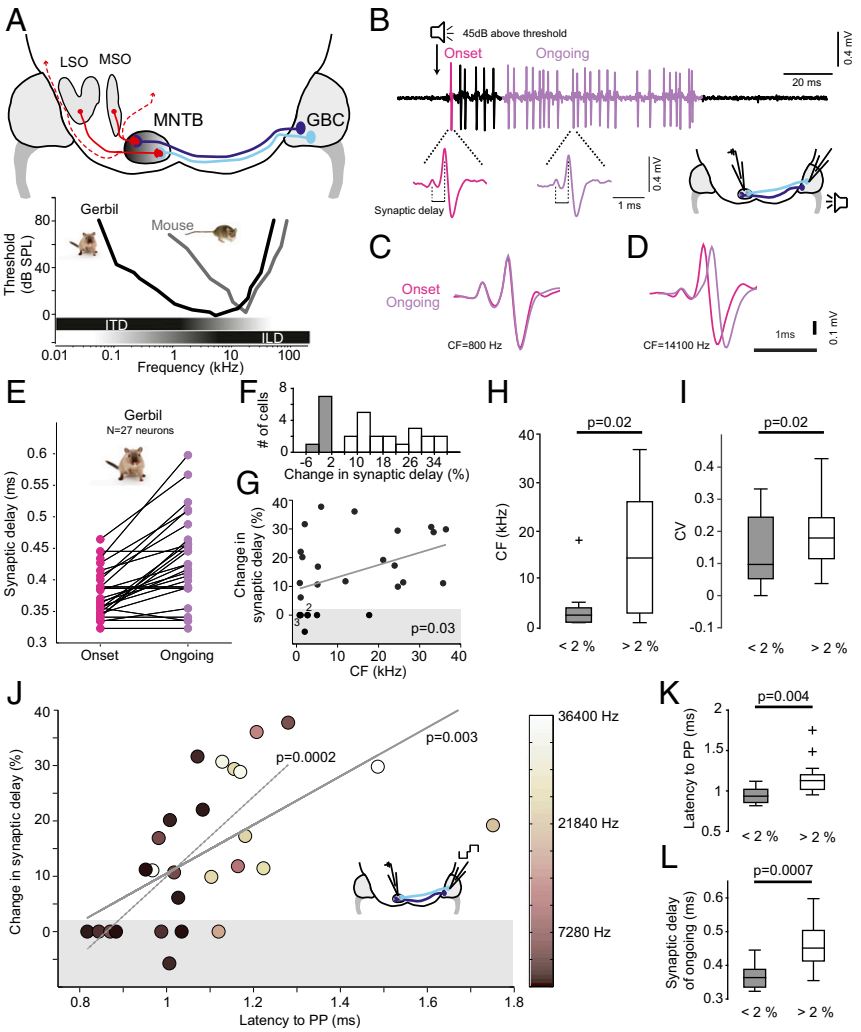

Fig. 1. Constant synaptic delays only in low-frequency-tuned, fast-conducting axons of gerbils. (*A*) Schematic of the mammalian sound localization circuits. Globular bushy cell (GBC) axons project to the contralateral medial nucleus of the trapezoid body (MNTB) to form one-to-one connections via the giant calyx of Held synapses. MNTB neurons then project to many brainstem and midbrain nuclei (dashed red lines), most importantly the lateral and medial superior olive (LSO and MSO, respectively) for binaural computation of sound source location: for high-frequency sounds, interaural level differences (ILDs) are analyzed in the LSO, whereas for low-frequency sounds—due to a lack of ILDs—interaural time differences (ITDs) are detected in the MSO. Both in gerbil and mouse, the MNTB is tonotopically organized with medially terminating GBC axons (light blue) tuned to higher, and laterally terminating axons (dark blue) tuned to lower frequencies. However, due to differences in the absolute hearing range (*Bottom*), the gerbil, but not the mouse, uses ITDs for sound localization. Typical frequency ranges of ITD and ILD processing are depicted by horizontal bars below the audiograms. (*B*) Representative example of sound-evoked responses of a single gerbil calyx-to-MNTB synapse/neuron (*Upper* trace). Below are blowups showing waveforms of the prepotential and the postsynaptic action potential to stimulus onset (pink) and to ongoing stimulus periods (purple). (*C*) Overlay of the waveforms recorded from a MNTB neuron tuned to low sound frequencies (CF = 800 Hz, the range where ITDs are used for sound localization), revealing identical synaptic delays (SDs) for onset (pink) and ongoing responses (purple). (*D*) Same display as in *C* for a neuron tuned to high sound frequencies (CF = 14,100 Hz), exhibiting the expected increase in SD. (*E*) Mean SD for onset (pink) and ongoing (purple) response plotted for each neuron recorded in the gerbil ($n = 27$). (*F*) Distribution of change in SD over the population of neurons ($n = 27$). Bins with stable SD (<2%) are denoted in gray. (*G*) The changes in SD significantly correlate ($P = 0.03$, Pearson correlation) with the postsynaptic MNTB neurons' CFs. Shaded area denotes stable SDs (changes <2%). (*H*) Neurons with stable SD (gray) show significantly lower CFs ($P = 0.02$, Mann–Whitney *U* test). Boxes indicate interquartile range with horizontal bar showing the median. Whiskers extend to the full data range, one outlier indicated by +. (*I*) Neurons with stable SD (gray) also had a significantly smaller coefficient of variation (CV) for ongoing SDs ($P = 0.02$, Mann–Whitney *U* test). Conventions are as in *H*. (*J*) Changes in SD strongly depend on the mean conduction latency of the presynaptic GBC axon ($P = 0.003$, Pearson correlation). The correlation did not depend on the two outliers with latencies >1.4 ms (dotted line, $P = 0.0002$, Pearson correlation). The CFs of the postsynaptic MNTB neurons are color coded. The conduction latency was measured by electric stimulation of GBC axons (see schematic). (*K* and *L*) In neurons with SD changes <2%, conduction latencies and absolute ongoing SDs are significantly shorter ($P = 0.004$ and $P = 0.0007$, respectively, Mann–Whitney *U* test) than for neurons with SD changes >2%. Conventions are as in *H*.

synaptic stage compared with the excitatory inputs to the MSO, both absolute and constant relative timing represents a key challenge for this circuit (5, 15, 22–24): Compared with onset information (i.e., action potential firing after longer periods of inactivity) passing through rested and thus less adapted calyx of Held synapses, inhibition would be progressively delayed relative to the excitation during ongoing activity by dozens to hundreds of microseconds due to the increase in synaptic delay (25). This activity-dependent increase in the overall delay of inhibition relative to excitation would corrupt the microsecond precision of inputs required for ITD processing. However, both at the level of single MSO neurons (26) as well as in human psychoacoustics (27), ITD detection does not differ between onset and ongoing sound components.

In addition to this problem of activity-dependent relative timing, ITD processing in MSO neurons is confronted by adapting the absolute timing of the individual inputs originating from the distinct pathways of different axonal lengths (ipsilateral vs. contralateral) and number of synapses. For example, contralateral inhibition via the GBCs and MNTB has been found to reliably precede the contralateral excitation by a few hundred microseconds despite its additional synapse (5, 22). We recently revealed structural adaptations in axonal caliber and the myelination pattern of GBC axons of Mongolian gerbils, providing an anatomical substrate for the observed temporal precedence of the inhibitory pathway (28). Intriguingly, we also discovered pronounced differences in axonal and myelin morphology within subpopulations of GBC axons tuned to low frequencies: although thicker in axon caliber, these GBC neurons exhibit shorter internode length, resulting in significantly faster conductance velocity and enhanced action potential precision (28). However, the MNTB targets not only MSO but many different auditory nuclei (29), including the LSO. It is therefore unclear whether differential myelination patterning and conduction velocity are specific adaptations for ITD processing or simply represent a general variation related to tonotopic organization per se.

Here, we observed activity-invariant relative input timing and examined whether the unusual myelination pattern observed in GBC fibers tuned to low frequencies is specifically related to ITD processing. To this end, we compared GBC axon morphology and synaptic transmission delays at the calyx of Held both in the Mongolian gerbil (an ITD user) and in the mouse (a non-ITD user). We found that the specializations in myelination and conduction velocity are highly specific to the functional requirements of ITD processing. We further revealed that explicitly in low-frequency tuned, fast conducting axons, the calyx of Held to MNTB synapse exhibited activity-invariant and thus stable delays.

Results

First we addressed the question of how activity-dependent increases of the synaptic transmission delay affect the relative timing of inhibition via the MNTB during sound location processing. Such increases would be detrimental for ITD processing in the MSO, where the additional calyx of Held synapse in the contralateral inhibitory pathway would introduce fluctuating and large (compared with the range of ITDs) changes in timing relative to the direct contralateral excitatory inputs. To determine the maximal range of increases that are introduced during high activity levels, we first measured in vivo the SD in the calyx of Held synapse of GBCs targeting MNTB principle neurons (Fig. 1 *A* and *B*). To study the specificity to ITD processing, we obtained these data both in gerbils, which possess both a well-developed MSO and LSO for ITD and ILD processing in the low- and high-frequency range, respectively, and mice, which possess only high-frequency hearing and are non-ITD users. We performed extracellular in vivo recordings of presynaptic potentials from the calyx of Held and the postsynaptic MNTB action potential (Fig. 1*B*) in response to 100-ms sound stimulation at each neuron's characteristic frequency (CF, the sound frequency a neuron responded best to) and rate-saturating intensity (45 dB above the neurons' threshold). To identify maximal changes in SD, we compared the mean SD of the first synaptic event related to the onset of an acoustic stimulus ("onset response") with the mean SD in the ongoing response (>20 ms after the onset response, when changes in SD are fully saturated).

In the gerbil, most cells showed the expected obvious increases in SD in this comparison but, surprisingly, some neurons exhibited no change in SDs (Fig. 1 *B–D*). Across all 27 neurons tested, the average SD in the onset response was 385.6 2 ± 46.2 μs (mean ± standard deviation) compared with 439.6 ± 73.0 μs (mean ± standard deviation) in the ongoing response (Fig. 1*E*). However, roughly one third of the neurons/synapses (8/27) did not exhibit any measurable increase in SD (<2%, Fig. 1*F*). More detailed analysis revealed a significant correlation of change of SD and sound-frequency tuning ($P = 0.03$, Pearson correlation, Fig. 1*G*). Particularly, fibers/neurons with stable SD tended to be tuned to lower sound-frequencies (SD change <2%: median CF, 2.35 kHz, 6/8 neurons with CF <3 kHz; SD change >2%: median CF, 14.1 kHz, $P = 0.02$, Mann–Whitney *U* test, Fig. 1*H*), and also exhibited less SD variance [coefficient of variation (CV)] (*Materials and Methods*) throughout the ongoing response component itself (SD change <2%: median CV, 0.097; SD change >2%: median CV, 0.18, $P = 0.02$, Mann–Whitney *U* test, Fig. 1*I*). The amount of change in SD correlated with firing rate in response to a CF pure tone (Fig. S1). Importantly, however, overall firing rate was not correlated with frequency tuning and, therefore, independent from phase locking (Fig. S1).

Low-frequency hearing requires ITD processing for sound localization, but not all low-frequency neurons necessarily need to be involved in ITD processing. To better characterize the properties of the recorded SDs, we also determined the conduction latency of the GBC axons that innervated the MNTB neurons by direct electrical stimulation (Fig. 1*J* and ref. 28). We noticed that neurons with the shortest absolute conduction latency (measured between peak of the stimulus artifact and peak of the prepotential) exhibited the smallest change of SD in the gerbil ($P = 0.003$, Pearson correlation; Fig. 1*J*, solid line; the correlation further increased to $P = 0.0002$ if two outliers were excluded; Fig. 1*J*, dashed line). Specifically, the fibers with stable SDs had significantly shorter conduction latencies ($P = 0.004$, Mann–Whitney *U* test, Fig. 1*K*) and shorter absolute ongoing SDs ($P = 0.0007$, Mann–Whitney *U* test, Fig. 1*L*) compared with fibers with >2% change in SD.

Taken together, in the gerbil, a subgroup of approximately 30% MNTB synapses exhibited constant SDs. These neurons were characterized by comparably lower CFs, shorter axonal conduction latencies, and shorter absolute SDs.

These data suggest that particularly those GBC axons and calyx of Held synapses that are specialized for faster and less variant action potential conduction and transmission are involved in ITD processing within the MSO circuit, where microsecond input precision is crucial. To test this hypothesis, we next repeated the SD measurements in the mouse, which does not use ITDs and thus would not require the specializations we found in the gerbil. We again obtained extracellular single cell recordings from the MNTB using the identical experimental protocol as for the gerbil. Overall, we found a similar overall trend of increasing SD when comparing onset (385.6 ± 46.2 μs, mean ± standard deviation) to ongoing responses (439.6 ±73.0 μs, mean ± standard deviation, Fig. 2*A*). However, in stark contrast to the gerbil data, there was only one single synapse/neuron in the mouse showing a change of SD smaller than 2% (Fig. 2 *B* and *C*). Moreover, changes of SDs in the mouse did not correlate with sound-frequency tuning ($P = 0.85$, Pearson correlation, Fig. 2*C*) or firing rate (Fig. S1). To facilitate comparisons with the gerbil data, where approximately 30% of the neurons exhibited stable SDs (Fig. 1*F*), we also compared the CV for ongoing SDs between the 30% of cells with the lowest changes in SD (corresponding to <5.5% change) and the remaining 70% of cells (>5.5% change in SD). In contrast to the gerbil, we found no difference in SD variance for mice between these groups (SD change <5.5%: median CV, 0.13; SD change >5.5%: median CV, 0.13; $P = 0.9$, Mann–Whitney *U* test; Fig. 2*D* and *Materials and Methods*). Finally, firing rate did not correlate with sound-frequency tuning (Fig. S1). Thus, activity-dependent changes in SD in the MNTB of mice were homogeneous across CF. A significant subpopulation with stable SDs was absent.

We had previously established that low-frequency GBC fibers in gerbils exhibit an unusual myelination pattern compared with high-frequency tuned fibers (Fig. 3, replotted from ref. 28) that results in significantly faster conduction velocity. Our physiological results suggest that specializations found in low-frequency fibers are specific to ITD processing. We thus hypothesized that

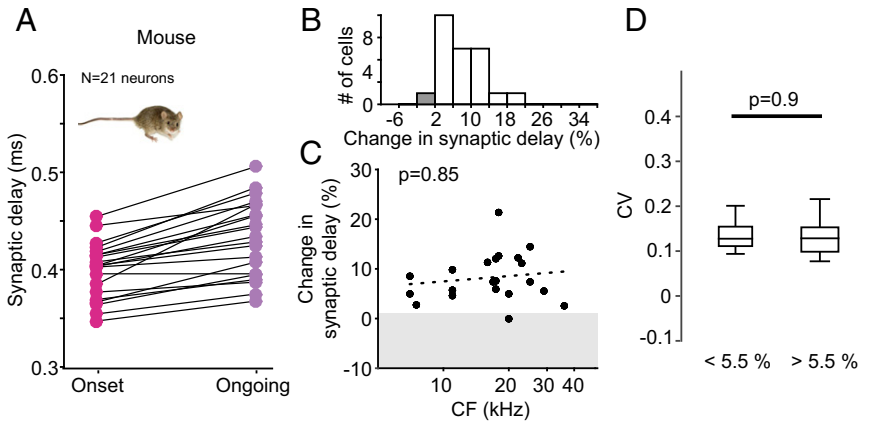

Fig. 2. Homogenous changes in synaptic delay across frequencies in mice. (*A*) Mean SDs for onset (pink) and ongoing (purple) responses plotted for each neuron recorded in the mouse ($n = 21$). (*B*) Distribution of change in SD over the population of neurons. Convention as in Fig. 1. (*C*) The changes in SD do not correlate ($P = 0.85$, Pearson correlation) with the postsynaptic MNTB neurons' CFs. Shaded area denotes stable SDs (changes <2%). Only one neuron falls into this group. (*D*) The coefficient of variation for the ongoing SDs is similar for all neurons irrespective of their change in SD ($P = 0.9$, Mann–Whitney *U* test). Conventions are as in Fig. 1*H*.

these morphological specializations might not be present in mouse GBC fibers. To address this question, we next compared myelination and fiber anatomy in low- and high-frequency GBC fibers in mice. We dye-filled GBC axons innervating the MNTB and counterstained against nodal and juxtaparanodal markers and then 3D-reconstructed single fibers starting from the calyx of Held synapse backward for multiple millimeters toward the GBC soma (Fig. 3*A*). We took advantage of the tonotopic arrangement of the MNTB and compared fibers terminating in the lateral third of the MNTB (GBClat, low frequency) to those terminating in the medial third of MNTB (GBCmed, high frequency) (Fig. 3*B*, *Left*). We quantified nodal and internodal axon diameter as well as internode length in five GBCmed and eight GBClat fibers (Fig. 3*B*, *Right*). Similar to our results from gerbils, the internode length in GBC fibers rapidly decreased close to the calyx of Held (Fig. 3*G*). However, mouse GBC fibers exhibited no significant differences in internodal axon diameter (mean ± SEM: GBCmed, 2.3 ± 0.1 μm; GBClat, 2.52 ± 0.08 μm; $P = 0.082$, two-sided *t* test, Fig. 3 *C* and *D*), node diameter (mean ± SEM: GBCmed, 1.58 ± 0.1 μm; GBClat, 1.5 ± 0.06 μm; $P = 0.51$, two-sided *t* test, Fig. 3 *E* and *F*) and internode length in the steady state part (>450 μm from heminode, mean ± SEM: GBCmed, 258.8 ± 19.1 μm; GBClat, 273.7 ± 17.9 μm; $P = 0.61$, two-sided *t* test, Fig. 3 *G* and *H*). Accordingly, there was also no significant difference in length/diameter (*L*/*d*) ratio (mean ± SEM: GBCmed, 123.0 ± 7.2 μm; GBClat, 130 ± 8.8 μm; $P = 0.58$, two-sided *t* test, Fig. 3 *I* and *J*). This finding is a remarkable contrast to the difference reported for GBCmed vs. GBClat values in the gerbil, which we obtained previously using identical methods and are depicted in Fig. 3 for comparison.

In gerbils, low-frequency/laterally terminating GBC fibers not only showed different myelination patterns but also significantly faster conductance velocity in vivo and in vitro (28). Therefore, we tested whether the lack of differences in GBC fibers in myelination in mice also correlated with a lack of difference in conduction velocity between GBClat and GBCmed axons. Electrical stimulation of GBC fibers at two different positions along the trapezoid tract (Fig. 3*K*, *Left*), causing pre- and postsynaptic events in the MNTB (Fig. 3*K*, *Right*), allowed us to measure absolute conduction speed in acute mouse brain slices ($n = 24$). In contrast to the gerbil, we found lateral ending fibers not to be faster than medially ending GBC fibers (Fig. 3*L*). In fact, faster fibers tended to terminate more medially ($P = 0.09$, Pearson correlation). Thus, in stark contrast to the gerbil, in the mouse, neither myelination patterning nor conduction speed showed any indication of specialized, faster conducting GBCs tuned to lower frequencies.

Together these data indicate that we have identified anatomical and physiological factors for the functionally specific tuning of temporally precise and stable tuning of inputs in circuit processing.

Discussion

The present study discovered structural and functional adaptations in the binaural auditory brainstem circuit. These adaptations facilitated stable and fast timing of inhibitory inputs via GBCs and the calyx of Held synapse onto MNTB glycinergic neurons. Most importantly, we revealed the presence of stable synaptic delays in a significant proportion of calyx of Held synapses in the gerbil, but not the mouse.

The GBC-to-MNTB pathway has already been known to incorporate a number of striking structural and functional adaptations for fast and reliable processing: the end bulb of Held (30, 31), superior phase locking in GBCs compared with their inputs (32), the calyx of Held giant synapse (18) and, discovered most recently, an unusual myelination pattern in GBCs tuned to lower frequencies associated with superior conductance velocity and temporal precision (28). We determined that in mice no such specializations in conduction velocity and precision were present, and mouse GBC axons conformed with standard internode length to axon caliber ratios irrespective of frequency tuning. We conclude that the inhibitory pathway involved in binaural processing of low-frequency sounds (<3 kHz) exhibits unique structural and functional adaptations for ultra-fast, precise, and temporally stable conduction and transmission as it is required for microsecond interaural time difference detection.

The presence of stable synaptic delays in a significant proportion of calyx of Held synapses in the gerbil appears to be a unique feature for chemical synapses in the central nervous system, at least to our knowledge. It is well established that chemical synapses, particularly the calyx of Held, rapidly adapt in transmission efficacy during ongoing activity (mice, rats, and gerbils) in vitro in acute brain slices (18, 33) as well as in vivo (34, 35). This adaptation is generally attributed to rapid changes in the available vesicle pool and calcium stores (36). One possible explanation for stable synaptic delays as described in the present study would be that these synapses resided in a highly pre-adapted stage, either through intrinsic mechanisms or due to constant high spontaneous activity (33). However, this seems unlikely to have been the case. First, probably due the choice of anesthetics, we encountered only little spontaneous activity that

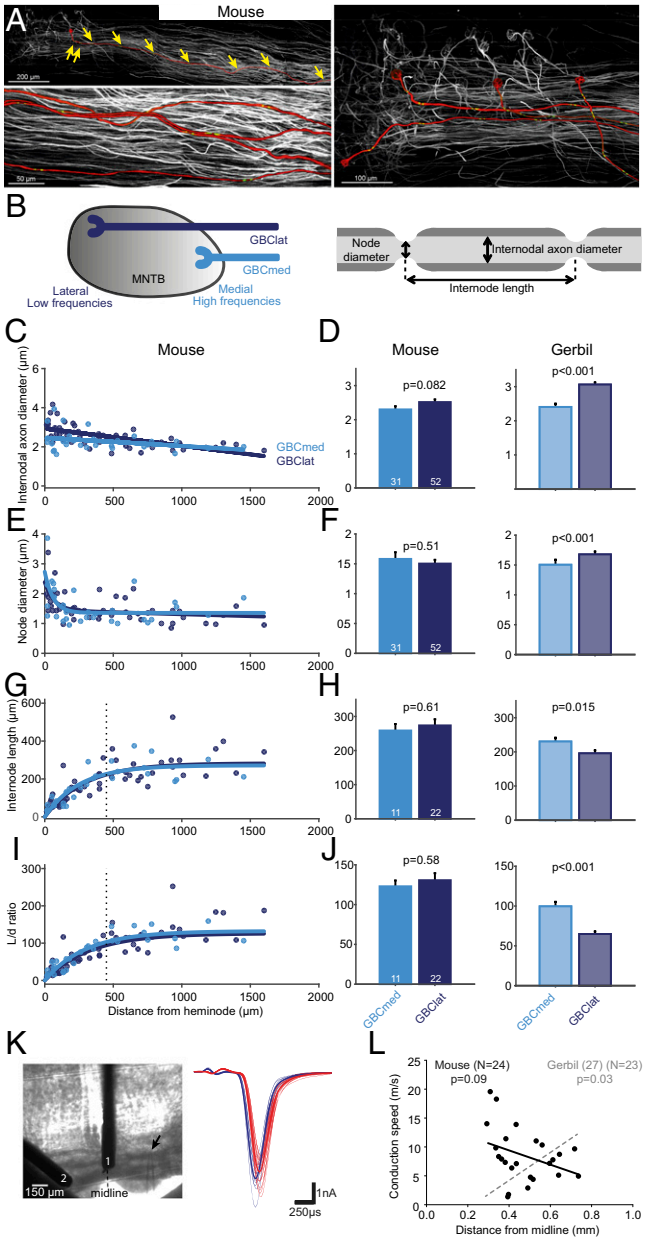

Fig. 3. Absence of structural and physiological specialization in mouse GBC axons. (*A*) Projections of confocal image stacks of mouse GBC axons innervating the MNTB filled with tetramethylrhodamine dextran. (*Top*, *Left*) One axon is highlighted in red and individual nodes of Ranvier are marked with yellow arrows. (*Bottom*, *Left*) Magnification of four axons; the position of juxtaparanodal (potassium Kv1.2) immunolabeled channels is shown in green. (*Right*) The tonotopic identity of axons was determined based on the relative position of calyces of Held along the mediolateral axis of the MNTB. (*B*) Schematic of the tonotopically organized MNTB (*Left*) and a myelinated axon illustrating the analyzed parameters (*Right*). (*C*, *E*, *G*, and *I*) Internodal axon diameter (*C*), node diameter (*E*), internode length (*G*), and internode length/internodal axon diameter (*L/d*) ratio (*I*) plotted against the distance from the heminode for lateral (GBClat, dark blue, $n = 8$ fibers) and medial (GBCmed, light blue, $n = 5$ fibers) terminating fibers. (*D*, *F*, *H*, and *J*) Averages of internodal axon diameter (*D*), node diameter (*F*), internode length (*H*), and *L/d* ratio (*J*) in GBCmed and GBClat fibers of mouse (*Left*) and gerbil (*Right*) (replotted from ref. 28). Data are represented as mean ± SEM. *P* values are derived from two-sided *t* tests (number of data points is given in bars). Vertical dashed line in *G* and *I* denotes beginning of steady-state section of internode length. Only steady-state values were used for calculation of the average in *H* and *J*. In stark contrast to the gerbil, no differences in axon morphology and myelination patterning between medially and laterally ending GBC fibers are present in the mouse. (*K*) Conduction velocity of mouse GBC fibers was measured by electrical stimulation at two different positions along the trapezoid tract (1, 2: stimulation electrodes, arrow demarks recording electrode, *Left*), eliciting excitatory postsynaptic currents (EPSCs) in the MNTB in vitro (blue and red EPSCs were elicited by stimulation electrodes 1 and 2, respectively, *Right*). (*L*) The mean conduction speed of GBC axons ($n = 24$) plotted against the mediolateral position of their terminating region in the MNTB. There is no significant correlation for mouse (black regression line), contrasting earlier findings from the gerbil (replotted from ref. 28 in gray).

was insufficient to generate such highly adapted states. More importantly, chronic synaptic adaptation would have caused maximal increases in synaptic delays. However, the subpopulation of synapses with stable synaptic delays we found in the gerbil exhibited significant shorter absolute synaptic delays during the ongoing phase compared with the neurons with nonstable synaptic delays, and thus it is highly unlikely that stable synaptic delays were caused by saturated adaptation before the onset response.

It is further known that the state of a neural network and, hence, anesthesia per se can influence aspects of synaptic short-term plasticity (37). However, differential direct effects of different anesthetics (used for mouse and gerbil) on synaptic adaptations and on synaptic delays in particular, have, to our knowledge, not been reported. Indirect differential effects due to hypothermia (38, 39) can be excluded here because body temperature in both mice and gerbils was tightly controlled. More importantly, the coherent increase of synaptic delays in the ongoing response in both mice and gerbils, and the fact that a very specific subset of synapses in the gerbil showed constant synaptic delays, strongly contradicts any differential effects due to anesthesia.

Insight into the potential mechanisms underlying stable synaptic delays in the MNTB may come from the ribbon synapse of inner hair cells, the only mammalian chemical synapse that also shows stable synaptic delays. Here it is well established that the unusual arrangement of vesicles in the ribbon and specialized proteins are required for fast docking and efficient exocytosis (40, 41). Moreover, specific short-latency calcium channels have been suggested to be involved in allowing rapid vesicle release also in the ongoing response (42) as well as calcium-induced calcium release from specific internal stores (43). Such mechanisms are likely to also play a role in the central nervous system including the MNTB (44). Differential calcium buffering has been suggested for lateral vs. medial calyx of Held synapses, which resulted in larger excitatory postsynaptic currents (EPSCs) in lateral MNTB neurons and might also contribute to more stable transmission in ongoing responses described in this present study (45). Additionally, an elevated state of release probability of synaptic vesicles, recently shown for the onset events in MNTB (46), may also be available in the ongoing response in neurons tuned to lower frequencies of the gerbil. However, because most research on the calyx of Held had been performed in mice or rats but not in ITD-using animals like gerbils (47) or guinea pigs (48), one can only speculate how constant synaptic delays are achieved in the subpopulation described above. A recent study even points to the importance of extracellular matrix, which can be found in the auditory brainstem and midbrain, for rapid synaptic release in the MNTB (49, 50). In any case, a multicausal explanation seems likely.

Functionally, stable synaptic delays seem to represent a specific adaptation for faithful ITD processing, because it would prevent fluctuations in the relative timing of direct excitation and indirect inhibition for responses to onsets vs. ongoing sounds in the range of tens to hundreds of microseconds. Such fluctuations may be negligible for most neuronal computations, but not for microsecond ITD processing of low-frequency sounds.

We have previously shown that in the MSO, ITD sensitivity for onset and ongoing is similar, which corroborates the idea that stable SDs are of functional importance for ITD processing (26). We and others have shown that the onset ITD dominates both perception as well as MSO processing if sharp rising transients are present in the envelope, which is the case for most natural sounds (51, 52).The importance of stable SD is, however, not limited to onset vs. ongoing responses: any changes in the activity level within tens of milliseconds will affect the synaptic delay (figure 5 in ref. 24). This effect is best demonstrated by comparing the onset and ongoing response components during our pure tone stimulation, but not limited to it, as the evaluation of CV for the ongoing SDs has shown, providing further evidence for the functional importance of constant synaptic delays for ITD processing.

Accordingly, stable synapses were, on average, tuned to low sound frequencies, had the shortest conduction latencies, and were characterized by minimal absolute synaptic delays. Most importantly, such synapses were lacking in an animal that does not hear low frequencies and does not use ITDs—the mouse. Whereas the correlation of constant synaptic delays and tuning to low-frequency sounds for the gerbil data were significant, a few high-frequency neurons also had constant synaptic delays and, conversely, a few low-frequency neurons did not. This spreading in the data may be accounted for by the functional variability of the system: Firstly, the MNTB neurons target not only LSO and MSO (15, 53–56), but also neurons in the superior paraolivary region (54, 57), and the monaural nuclei of the lateral lemniscus (57–59). Moreover, low-frequency LSO neurons exhibit trough-type ITD sensitivity, which has only small response modulation within the physiological range of ITDs and mainly in the periphery of auditory space (60). Hence, subpopulations of the low-frequency MNTB cells contribute to a variety of circuits and computations that do not require submillisecond timing precision. Secondly, mammals that developed low-frequency ITD processing can also detect ITDs in the envelope of high-frequency sounds, albeit to a lesser extent and with inferior accuracy (13, 51, 61). Thus, a subgroup of high-frequency tuned neurons in the gerbil involved in ITD processing is actually not unexpected.

There is good evidence from gerbils that inhibitory inputs to the MSO via the MNTB precede the direct excitatory input originating at the same contralateral cochlear nucleus (5, 22), which is remarkable, given that the inhibitory pathway involves the additional calyx of Held synapse. Recently we showed that the inhibitory pathway conquers this challenge via a two- to threefold thicker axon diameter of GBCs compared with the spherical bushy cells, which comprise the excitatory input (28). Moreover, we revealed the presence of a dramatic decrease of internode length toward the terminal region in both fiber classes. Our present study clarifies that this decrease is a universal feature (at least) of GBC fibers irrespective of species, as a similar decrease in internode length was also found in the mouse. We also previously established that gerbil GBC fibers tuned to low frequencies exhibited an unusual myelination pattern that strongly deviated from the canonical concept of constant internode length to axon diameter ratios of ~100. Although even thicker in axon caliber than high-frequency fibers, these axons exhibit shorter internode length, resulting in internode length/diameter ratios of only ~60 (Fig. 3 and ref. 28). It remained unclear, however, whether this unusual structural feature relates to relative low frequencies within the tonotopic organization of the auditory pathway per se or specifically to absolute low-frequency hearing. The fact that we found "normal" myelination patterns throughout the tonotopic axis in the mouse strongly suggested the latter and thus identifies the morphological specializations in gerbils as adaptations that are specific to ITD processing. It follows that a preceding of inhibition relative to excitation might be of crucial relevance for the computation of ITDs (5, 26). Although the exact way the different MSO inputs are integrated to realize ITD resolution of about 30 μs on a single cell level is still highly controversial (22, 62–64), there is evidence for extraordinary temporal precision of the glycinergic MNTB input to the MSO including an experience-driven developmental selection of very few but strong inputs that show fast inhibitory postsynaptic currents (IPSCs)/inhibitory postsynaptic potentials (IPSPs). Our findings of morphological and physiological specializations in the inhibitory pathway strongly corroborate that not only fast, but precisely timed inhibition to the MSO is of central importance for the ITD processing mechanism.

Materials and Methods

All experiments were approved in accordance with the stipulations of the German animal welfare law (Tierschutzgesetz) (AZ 55.2–1-54.2531.8–211-10). Animals were housed in groups of four to six individuals with 12-h light/dark cycles.

Depending on normality of the distribution, population average data are shown by the mean ± SEM, or the median and the 25% and 75% confidence intervals as box edges with full data ranges depicted by whiskers. Accordingly, parametric or nonparametric tests were used to determine statistical significances. No blinding was done for data analysis; however, identical automated code was used for analysis of all data.

In Vivo Measurements of Synaptic Delays in MNTB and GBC Latency. Identification of MNTB neurons and their GBC input during recordings was assured by the fact that voltage volleys ("prepotentials") were observed preceding the postsynaptic action potential for all neurons included in the dataset. Prepotentials are generated by the giant calyx of Held and thus a clear characteristic of MNTB recordings (65, 66). Likewise, the fact that MNTB neurons receive their calycal input only from GBCs positively identified the anatomical identity of the recorded neurons and presynaptic partner (19, 67, 68).

Gerbil. Methods for part of the dataset were described in detail previously (28). In short, 14 adult [postnatal age (P) 60–120] Mongolian gerbils (*Meriones unguiculatus*) of both sexes were initially anesthetized with an i.p. injection (0.5 mL/100 g body weight) of a mixture of ketamine (20%) and xylazine (2%) diluted in 0.9% NaCl solution. During recording, animals were injected continuously with the same anesthesia via an automatic pump (801 Syringe Pump, Univentor) at a pump rate of 1.6–2.5 μL/min depending on body weight and state of anesthesia, which was measured using the toe pinch reflex. Each animal was mounted in a custom-made stereotaxic instrument (69) that was located in a sound-attenuated chamber, and constant body temperature was maintained at 37 °C. The MNTB was accessed by a craniotomy lateral to the midline above the lambda suture, and the anterior ventral cochlear nucleus (AVCN) by a craniotomy lateral to the midline caudal to the posterior aspect of the transverse sinus. After recording, the animal was killed with pentobarbital (20 mg/mL).

Neurons in the MNTB were acoustically and electrically stimulated and single-unit responses were recorded extracellularly with glass electrodes (3–37 MΩ) filled with 3 M KCl. Recordings were preamplified (patch clamp EPC 10 USB, HEKA), filtered (Humbug 50/60 Hz noise eliminator, Quest Scientific), and fed to a computer via a Multi I/O processor (RZ6, Tucker-Davies Technology). The voltage traces were digitized at a sampling rate of 48 kHz and band-pass filtered (0.4–6 kHz). Only neurons with characteristic complex waveforms, consisting of a prepotential and a postsynaptic spike as typical for the MNTB were included.

Acoustic stimuli were digitally generated at a sampling rate of 200 kHz by TDT System III (Tucker-Davies Technology), digitally attenuated, and converted to analog signals (RZ6, Tucker-Davies Technology), and then delivered to earphones (ER 4PT, Etymotic Research). Responses to monaural stimulation with pure tones (100-ms duration plus 5-ms cosine rise/fall time) of predefined frequency/intensity combinations (6 intensities and 9 frequencies, >5 repetitions) were used to determine the CF of the MNTB neuron. Subsequently, pure tones (100-ms duration plus 5-ms cosine rise/fall time) at CF and 11 different sound intensities (5 dB below to 45 dB above threshold, at least 15 repetitions), with 120-ms interstimulus interval were presented to measure SD. The mean SD of the first spike of each repetition was compared with the mean SD of the ongoing spikes at a sound intensity of 45 dB above threshold. Only spikes occurring >20 ms after the initial response were included into the calculation of the mean ongoing SD, as the increase in SD is maximally saturated at this time (25). Values are shown as mean and used to calculate the relative change in synaptic delay. The CV of the ongoing response was calculated by dividing the SD of SDs for all spikes occurring >20 ms (for the 4 highest intensities recorded) by the mean SD. Electric stimuli were biphasic cathodic leading current pulses (120 μs per phase, 40-μs

interphase gap, 2 Hz repeat rate, 0–40 μA amplitude in 2-μA steps, >10 repetitions), that were digitally generated at a sampling frequency of 25 kHz and passed to the electrode channels (RX7-2 stimulator base station and MS16 stimulus isolator, Tucker-Davies Technology) of a 16-channel tungsten electrode microwire array (Omnetics-based electrodes, Tucker-Davies Technology). The time period between the peak of the stimulation artifact and the peak of the prepotential was measured to calculate the axonal action potential propagation latency.

Data analysis was performed by custom-made code in Matlab (Mathworks).

Mouse. Five CBA/J mice (P92–P105) of both sexes were used for in vivo recordings. The mice were anesthetized with a s.c. injection of 0.01 mL/g medetomidine-midazolam-fentanyl (MMF) (0.5 mg/kg body weight medetomidine, 5.0 mg/kg body weight midazolam, and 0.05 mg/kg body weight fentanyl). Depth of anesthesia was measured using the toe pinch reflex and responding animals were given supplemental MMF at one-third the initial dose. Anesthesia was maintained using this method for the duration of the experiment. The mice were placed in an experimental setup identical to that described for the gerbils. To access the MNTB, a craniotomy was performed at the rostrocaudal midpoint of the interparietal skull plate lateral to the midline and extracellular responses were recorded with glass electrodes (5–20 MΩ) filled with 3 M KCl. Signals were amplified (Neuroprobe Amplifier Model 1600, A-M Systems), filtered (300–3,000 Hz; Tucker-Davies Technology model PC1) and recorded (~50-kHz sampling rate) with an RZ6 processor (Tucker-Davies Technology) and SPIKE software (Brandon Warren, V. M. Bloedel Hearing Research Center, University of Washington, Seattle, WA). Acoustic stimuli were digitally generated as described for gerbil with SPIKE software and then delivered to earphones (MF1, Tucker-Davies Technology). After recording, the animal was killed with pentobarbital (20 mg/mL). Data for synaptic delay measures were collected and analyzed in a way identically to that described for gerbils. The CV of the ongoing response was calculated by dividing the SD of SDs for all spikes occurring >20 ms by the mean SD.

In Vitro Measurements of Axonal Conduction Velocity. Sixteen CBA/Ca mice of either sex (P16–P35) were anesthetized with isoflurane and killed by decapitation. Coronal brainstem sections (200 μm thick) containing the superior olivary complex were cut in an ice-cold high-sucrose, low-sodium artificial cerebral spinal fluid (ACSF) as previously reported (70). Brainstem slices were maintained after slicing in normal ACSF at 37 °C for 30–45 min, after which they were stored in a slice-maintenance chamber at room temperature (~22 °C). Composition of the normal ACSF (in millimoles): 125 NaCl, 2.5 KCl, 26 $NaHCO_3$, 10 glucose, 1.25 NaH_2PO_4, 2 sodium pyruvate, 3 myo-inositol, 2 $CaCl_2$, 1 $MgCl_2$, and 0.5 ascorbic acid, pH = 7.4, bubbled with 95% O_2 and 5% CO_2. For the low-sodium ACSF, $CaCl_2$ and $MgCl_2$ concentrations were 0.1 and 4 mM, respectively, and NaCl was replaced by 200 mM sucrose. Experiments were conducted at 36 ± 1 °C, maintained by an inline feedback temperature controller and heated stage (TC344B, Warner Instruments) with the recording chamber being continuously perfused with ACSF at a rate of 1–2 mL·min^{-1}. Whole-cell patch-clamp recordings were made from visually identified MNTB neurons (Olympus BX51WI microscope) using an EPC10/2HEKA amplifier, sampling at 50 kHz, and filtering between 2.9 and 10 kHz. Patch pipettes were filled with a patch solution containing (in millimoles): 126 K-gluconate, 4 KCl, 40 Hepes, 5 EGTA, 1 $MgCl_2$, 5 Na_2 phosphocreatine, 0.2% biocytin, and 292 mOsm, (all chemicals from Sigma-Aldrich), pH = 7.2. Electrode resistance was between 2.4 and 6 MΩ. Synaptic potentials were evoked by afferent fiber stimulation with two concentric bipolar electrodes (FHC, Inc.) pushed gently onto the surface of the trapezoid body, one over the midline and another on the contralateral side to the recording patch electrode near the LSO. The latencies of responses were compared and used to calculate conduction speed (28). Voltage pulses were generated by the HEKA amplifier and postamplified by a linear stimulus isolator (PulseStimulator AM-2100). The contralateral electrode was moved around the slice to attain the lowest voltage threshold for stimulation. Latencies for the conduction speed measurements were obtained from the onset of the stimulus artifact to the half-maximum of the postsynaptic response. For each cell, a minimum of nine EPSCs was obtained from each electrode to generate a mean value for EPSC latency in response to stimulation at threshold. Only EPSCs greater than 1 nA were considered calyceal and used for analysis. No explicit information about the caliber size of the stimulated axons was obtainable. However, the largest caliber axons within the trapezoid body have previously been shown to be the GBC axons, which provide MNTB input (71, 72). The distance between the tip of the recording electrode and the midline of the slice and the distance between the tip of the recording electrode and the stimulation electrodes were measured using ImageJ (73).

The conduction speed data here form part of a dataset examining the development of conduction of trapezoid body fibers in mouse.

In Vitro Axon Tracing. Five CBA/Ca mice both sexes aged P25–P30 were deeply anesthetized with pentobarbital (2 mg/kg body weight) and intracardially perfused with ice-cold Ringer's solution containing heparin. After decapitation, the brainstem was quickly removed from the skull under ice-cold ACSF comprising (in millimoles): 125 NaCl, 2.5 KCl, 1 $MgCl_2$, 2 $CaCl_2$, 10 glucose, 1.25 NaH_2PO_4, 26 $NaHCO_3$, 0.5 ascorbic acid, 3 myo-inositol, and 2 pyruvic acid (all chemicals from Sigma-Aldrich). For anterograde tracing of GBC axons, borosilicate micropipettes with a tip diameter of 10–15 μm were filled with a 10% solution of tetramethylrhodamine dextran (3,000 molecular weight; Invitrogen D-3308) and visually guided to the AVCN in brainstem explants using a stereomicroscope. Tracer was pressure injected (15 pounds per square inch) into the GBC area of the AVCN using a picospritzer (Picospritzer III, Parker), followed by several electroporation pulse trains (50-ms pulses at 50 V and 10-Hz repetition rate) using an isolated pulse stimulator (A-M Systems). Subsequently, the explants were transferred to a chamber with oxygenated ACSF and incubated for 2.5 h at room temperature to allow for homogeneous distribution of the tracer in axons. Thereafter, the brainstems were immersion fixed for 2 h at room temperature, and followed overnight at 4 °C in 4% paraformaldehyde solution.

Immunohistochemistry and Confocal Microscopy. Brainstems were sectioned coronally at 120 μm using a vibratome slicer. Immunostaining was carried out as described (28). Primary antibodies for Kv1.2 (NeuroMab; 75-008 clone K14/16; mouse IgG2b; 1:500) and corresponding secondary antibodies (donkey anti-mouse Alexa-488, Dianova) and Fluorescent Nissl BlueTracer (Invitrogen) were applied. Confocal optical sections were acquired with a Leica TCS SP5-2 confocal laser-scanning microscope (Leica Microsystems) equipped with HCX PL APO X63/numerical aperture 1.3 glycerol 37 °C objective. Fluorochromes were visualized with excitation wavelengths of 405 nm (emission filter, 410–430 nm) for Nissl Blue, 488 nm (emission filter, 510–540 nm) for Alexa-488, 561 nm (emission filter, 565–585 nm) for tetramethylrhodamine dextran. Overlapping stacks of images were acquired from coronal brainstem slices (120 μm thick) at the level of the trapezoid body in the area spanning the MNTB and the contralateral tracer injection site (cochlear nucleus); voxel size: 482 × 482 × 290 nm. Red-green-blue (RGB) stacks, montages of RGB optical sections, and maximum-intensity projections were assembled using the ImageJ 1.37 k plugins and Adobe Photoshop 8.0.1 (Adobe Systems) software. GBC fibers were identified by calyces of Held that terminated in the contralateral MNTB and then back tracked across sections toward the cochlear nucleus. On the basis of their exact site of termination in the MNTB, GBC axons were classified as being either medially or laterally terminating. MNTB borders were determined using a counterstain (fluorescent Nissl stain). Morphometric analysis was carried out as described before for gerbil GBC axons (28).

ACKNOWLEDGMENTS. The authors thank Marc C. Ford for discussions and assistance with morphological data analysis. This work was supported by the German Research Association (DFG) Collaborative Research Center (870, B02 to B.G. and M.P. and A10 to C.K.-S.) and Priority Program (1608 to M.P.).

1. Sun YJ, et al. (2010) Fine-tuning of pre-balanced excitation and inhibition during auditory cortical development. *Nature* 465:927–931.
2. Wehr M, Zador AM (2003) Balanced inhibition underlies tuning and sharpens spike timing in auditory cortex. *Nature* 426:442–446.
3. Pecka M, Han Y, Sader E, Mrsic-Flogel TD (2014) Experience-dependent specialization of receptive field surround for selective coding of natural scenes. *Neuron* 84:457–469.
4. Pouille F, Scanziani M (2001) Enforcement of temporal fidelity in pyramidal cells by somatic feed-forward inhibition. *Science* 293:1159–1163.
5. Brand A, Behrend O, Marquardt T, McAlpine D, Grothe B (2002) Precise inhibition is essential for microsecond interaural time difference coding. *Nature* 417:543–547.
6. Barrett EF, Stevens CF (1972) The kinetics of transmitter release at the frog neuromuscular junction. *J Physiol* 227:691–708.
7. Katz B, Miledi R (1965) The measurement of synaptic delay, and the time course of acetylcholine release at the neuromuscular junction. *Proc R Soc Lond B Biol Sci* 161:483–495.
8. Wu LG, Borst JG (1999) The reduced release probability of releasable vesicles during recovery from short-term synaptic depression. *Neuron* 23:821–832.
9. Fedchyshyn MJ, Wang L-Y (2007) Activity-dependent changes in temporal components of neurotransmission at the juvenile mouse calyx of Held synapse. *J Physiol* 581:581–602.
10. Stuart GJ, Spruston N (2015) Dendritic integration: 60 years of progress. *Nat Neurosci* 18:1713–1721.
11. Krächan EG, Fischer AU, Franke J, Friauf E (2017) Synaptic reliability and temporal precision are achieved via high quantal content and effective replenishment: Auditory brainstem versus hippocampus. *J Physiol* 595:839–864.

12. Sawtell NB, Williams A, Bell CC (2005) From sparks to spikes: Information processing in the electrosensory systems of fish. *Curr Opin Neurobiol* 15:437–443.
13. Grothe B, Pecka M, McAlpine D (2010) Mechanisms of sound localization in mammals. *Physiol Rev* 90:983–1012.
14. Golding NL, Oertel D (2012) Synaptic integration in dendrites: Exceptional need for speed. *J Physiol* 590:5563–5569.
15. Grothe B, Sanes DH (1994) Synaptic inhibition influences the temporal coding properties of medial superior olivary neurons: An in vitro study. *J Neurosci* 14:1701–1709.
16. Boudreau JC, Tsuchitani C (1968) Binaural interaction in the cat superior olive S segment. *J Neurophysiol* 31:442–454.
17. Grothe B, Pecka M (2014) The natural history of sound localization in mammals: A story of neuronal inhibition. *Front Neural Circuits* 8:116.
18. von Gersdorff H, Borst JGG (2002) Short-term plasticity at the calyx of Held. *Nat Rev Neurosci* 3:53–64.
19. Smith PH, Joris PX, Carney LH, Yin TC (1991) Projections of physiologically characterized globular bushy cell axons from the cochlear nucleus of the cat. *J Comp Neurol* 304:387–407.
20. Tollin DJ (2003) The lateral superior olive: A functional role in sound source localization. *Neuroscientist* 9:127–143.
21. Grothe B (2003) New roles for synaptic inhibition in sound localization. *Nat Rev Neurosci* 4:540–550.
22. Roberts MT, Seeman SC, Golding NL (2013) A mechanistic understanding of the role of feedforward inhibition in the mammalian sound localization circuitry. *Neuron* 78: 923–935.
23. Roberts MT, Seeman SC, Golding NL (2014) The relative contributions of MNTB and LNTB neurons to inhibition in the medial superior olive assessed through single and paired recordings. *Front Neural Circuits* 8:49.
24. Joris PX, Smith PH (2008) The volley theory and the spherical cell puzzle. *Neuroscience* 154:65–76.
25. Tolnai S, Englitz B, Scholbach J, Jost J, Rübsamen R (2009) Spike transmission delay at the calyx of Held in vivo: Rate dependence, phenomenological modeling, and relevance for sound localization. *J Neurophysiol* 102:1206–1217.
26. Pecka M, Brand A, Behrend O, Grothe B (2008) Interaural time difference processing in the mammalian medial superior olive: The role of glycinergic inhibition. *J Neurosci* 28:6914–6925.
27. Blauert J (1997) *Spatial Hearing: The Psychophysics of Human Sound Localization* (MIT Press, Cambridge, MA).
28. Ford MC, et al. (2015) Tuning of Ranvier node and internode properties in myelinated axons to adjust action potential timing. *Nat Commun* 6:8073.
29. Kulesza RJ, Jr, Grothe B (2015) Yes, there is a medial nucleus of the trapezoid body in humans. *Front Neuroanat* 9:35.
30. Pliss L, Yang H, Xu-Friedman MA (2009) Context-dependent effects of NMDA receptors on precise timing information at the endbulb of Held in the cochlear nucleus. *J Neurophysiol* 102:2627–2637.
31. Yang H, Xu-Friedman MA (2009) Impact of synaptic depression on spike timing at the endbulb of Held. *J Neurophysiol* 102:1699–1710.
32. Joris PX, Carney LH, Smith PH, Yin TC (1994) Enhancement of neural synchronization in the anteroventral cochlear nucleus. I. Responses to tones at the characteristic frequency. *J Neurophysiol* 71:1022–1036.
33. Hermann J, Pecka M, von Gersdorff H, Grothe B, Klug A (2007) Synaptic transmission at the calyx of Held under in vivo like activity levels. *J Neurophysiol* 98:807–820.
34. Englitz B, Tolnai S, Typlt M, Jost J, Rübsamen R (2009) Reliability of synaptic transmission at the synapses of Held in vivo under acoustic stimulation. *PLoS One* 4:e7014.
35. Kopp-Scheinpflug C, Lippe WR, Dörrscheidt GJ, Rübsamen R (2003) The medial nucleus of the trapezoid body in the gerbil is more than a relay: Comparison of pre- and postsynaptic activity. *J Assoc Res Otolaryngol* 4:1–23.
36. Borst JGG, Soria van Hoeve J (2012) The calyx of Held synapse: From model synapse to auditory relay. *Annu Rev Physiol* 74:199–224.
37. Reig R, Sanchez-Vives MV (2007) Synaptic transmission and plasticity in an active cortical network. *PLoS One* 2:e670.
38. Hume AL, Durkin MA (1986) Central and spinal somatosensory conduction times during hypothermic cardiopulmonary bypass and some observations on the effects of fentanyl and isoflurane anesthesia. *Electroencephalogr Clin Neurophysiol* 65:46–58.
39. Charlet de Sauvage R, da Costa DL, Erre JP, Aran JM (1996) Changes in CM and CAP with sedation and temperature in the guinea pig: Facts and interpretation. *Hear Res* 102:15–27.
40. Wichmann C, Moser T (2015) Relating structure and function of inner hair cell ribbon synapses. *Cell Tissue Res* 361:95–114.
41. Trapani JG, Obholzer N, Mo W, Brockerhoff SE, Nicolson T (2009) Synaptojanin1 is required for temporal fidelity of synaptic transmission in hair cells. *PLoS Genet* 5: e1000480.
42. Zampini V, et al. (2013) Burst activity and ultrafast activation kinetics of CaV1.3 Ca^{2+} channels support presynaptic activity in adult gerbil hair cell ribbon synapses. *J Physiol* 591:3811–3820.
43. Castellano-Muñoz M, Ricci AJ (2014) Role of intracellular calcium stores in hair-cell ribbon synapse. *Front Cell Neurosci* 8:162.
44. Lin KH, Taschenberger H, Neher E (2017) Dynamics of volume-averaged intracellular Ca(2+) in a rat CNS nerve terminal during single and repetitive voltage-clamp depolarizations. *J Physiol* 595:3219–3236.
45. Weatherstone JH, et al. (2016) Maintenance of neuronal size gradient in MNTB requires sound-evoked activit. *J Neurophysiol* 117:756–766.
46. Taschenberger H, Woehler A, Neher E (2016) Superpriming of synaptic vesicles as a common basis for intersynapse variability and modulation of synaptic strength. *Proc Natl Acad Sci USA* 113:E4548–E4557.
47. Lesica NA, Lingner A, Grothe B (2010) Population coding of interaural time differences in gerbils and barn owls. *J Neurosci* 30:11696–11702.
48. McAlpine D, Jiang D, Palmer AR (2001) A neural code for low-frequency sound localization in mammals. *Nat Neurosci* 4:396–401.
49. Blosa M, et al. (2015) The extracellular matrix molecule brevican is an integral component of the machinery mediating fast synaptic transmission at the calyx of Held. *J Physiol* 593:4341–4360.
50. Hilbig H, Nowack S, Boeckler K, Bidmon H-J, Zilles K (2007) Characterization of neuronal subsets surrounded by perineuronal nets in the rhesus auditory brainstem. *J Anat* 210:507–517.
51. Dietz M, Marquardt T, Salminen NH, McAlpine D (2013) Emphasis of spatial cues in the temporal fine structure during the rising segments of amplitude-modulated sounds. *Proc Natl Acad Sci USA* 110:15151–15156.
52. Dietz M, et al. (2014) Emphasis of spatial cues in the temporal fine structure during the rising segments of amplitude-modulated sounds II: Single-neuron recordings. *J Neurophysiol* 111:1973–1985.
53. Moore MJ, Caspary DM (1983) Strychnine blocks binaural inhibition in lateral superior olivary neurons. *J Neurosci* 3:237–242.
54. Kuwabara N, Zook JM (1991) Classification of the principal cells of the medial nucleus of the trapezoid body. *J Comp Neurol* 314:707–720.
55. Kapfer C, Seidl AH, Schweizer H, Grothe B (2002) Experience-dependent refinement of inhibitory inputs to auditory coincidence-detector neurons. *Nat Neurosci* 5: 247–253.
56. Zarbin MA, Wamsley JK, Kuhar MJ (1981) Glycine receptor: Light microscopic autoradiographic localization with [3H]strychnine. *J Neurosci* 1:532–547.
57. Sommer I, Lingenhöhl K, Friauf E (1993) Principal cells of the rat medial nucleus of the trapezoid body: An intracellular in vivo study of their physiology and morphology. *Exp Brain Res* 95:223–239.
58. Spangler KM, Warr WB, Henkel CK (1985) The projections of principal cells of the medial nucleus of the trapezoid body in the cat. *J Comp Neurol* 238:249–262.
59. Smith PH, Joris PX, Yin TC (1998) Anatomy and physiology of principal cells of the medial nucleus of the trapezoid body (MNTB) of the cat. *J Neurophysiol* 79: 3127–3142.
60. Tollin DJ, Yin TCT (2005) Interaural phase and level difference sensitivity in low-frequency neurons in the lateral superior olive. *J Neurosci* 25:10648–10657.
61. Bernstein LR (2001) Auditory processing of interaural timing information: new insights. *J Neurosci Res* 66:1035–1046.
62. Franken TP, Bremen P, Joris PX (2014) Coincidence detection in the medial superior olive: Mechanistic implications of an analysis of input spiking patterns. *Front Neural Circuits* 8:42.
63. van der Heijden M, et al. (2013) Directional hearing by linear summation of binaural inputs at the medial superior olive. *Neuron* 78:936–948.
64. Myoga MH, Lehnert S, Leibold C, Felmy F, Grothe B (2014) Glycinergic inhibition tunes coincidence detection in the auditory brainstem. *Nat Commun* 5:3790.
65. Guinan JJ, Jr, Li RY (1990) Signal processing in brainstem auditory neurons which receive giant endings (calyces of Held) in the medial nucleus of the trapezoid body of the cat. *Hear Res* 49:321–334.
66. Mc Laughlin M, van der Heijden M, Joris PX (2008) How secure is in vivo synaptic transmission at the calyx of Held? *J Neurosci* 28:10206–10219.
67. Spirou GA, Brownell WE, Zidanic M (1990) Recordings from cat trapezoid body and HRP labeling of globular bushy cell axons. *J Neurophysiol* 63:1169–1190.
68. Kuwabara N, DiCaprio RA, Zook JM (1991) Afferents to the medial nucleus of the trapezoid body and their collateral projections. *J Comp Neurol* 314:684–706.
69. Schuller G, Radtke-Schuller S, Betz M (1986) A stereotaxic method for small animals using experimentally determined reference profiles. *J Neurosci Methods* 18:339–350.
70. Barnes-Davies M, Forsythe ID (1995) Pre- and postsynaptic glutamate receptors at a giant excitatory synapse in rat auditory brainstem slices. *J Physiol* 488:387–406.
71. Morest DK (1968) The collateral system of the medial nucleus of the trapezoid body of the cat, its neuronal architecture and relation to the olivo-cochlear bundle. *Brain Res* 9:288–311.
72. Brownell WE (1975) Organization of the cat trapezoid body and the discharge characteristics of its fibers. *Brain Res* 94:413–433.
73. Schneider CA, Rasband WS, Eliceiri KW (2012) NIH Image to ImageJ: 25 years of image analysis. *Nat Methods* 9:671–675.